

HETEROGENEOUS LOWERMOST MANTLE: COMPOSITIONAL CONSTRAINTS AND SEISMOLOGICAL OBSERVABLES

H. Samuel ¹

Laboratoire de Dynamique des Systèmes Géologiques, Institut de Physique du Globe de Paris, Paris, France

C. G. Farnetani

Laboratoire de Dynamique des Systèmes Géologiques, Institut de Physique du Globe de Paris, Paris, France

D. Andraut

Institut de Minéralogie et de Physique des Milieux Condensés, Paris, France

Several seismological observations indicate the existence of compositional heterogeneities in the lowermost mantle, in particular, the anticorrelation between bulk sound and shear wave velocity anomalies, and anomalously high values (i.e., > 2.7) of the ratio $R = d\ln V_S/d\ln V_P$. Constraining the composition of such heterogeneous material is fundamental to determine its origin and its possible role on the dynamical evolution of the Earth's mantle. In this paper we propose a new approach to constrain the composition of chemically denser material in the lower mantle. Using geodynamical and seismological constraints we show that the denser material has to be enriched in both iron and silica with respect to a pyrolitic lower mantle. The required enrichment is reduced if we consider that at high pressure Al-perovskite decreases the iron-magnesium partition coefficient between magnesiowüstite and perovskite. We then apply the estimated composition to the distribution of chemical heterogeneities calculated by our thermo-chemical convection model. In the deep mantle we predict broad seismic velocity anomalies and strong lateral velocity variations. Moreover, we find that areas of anticorrelation are associated with upwelling mantle flow, in agreement with tomographic studies. The calculated R ratio varies laterally and may locally have values greater than 2.7, often associated with areas of anticorrelation. Our results compare well with seismic observations and provide a way to reconcile apparent discrepancies between global tomographic models. Finally, we suggest that only an enrichment in iron and silica in the lowermost mantle is required to explain seismological observations.

¹Now at Department of Geology and Geophysics, Yale University, New Haven, USA

1. INTRODUCTION

Seismic tomography is a powerful tool for imaging the Earth's deep mantle structure. Despite technical differences (i.e., data treatment procedures, parametrization, and inversion method) tomographic models display many common features, for example, the increase of the Root Mean Square (RMS) of body waves seismic velocity anomalies below a depth of 2000 km [Grand *et al.*, 1997; Kennett *et al.*, 1998; Masters *et al.*, 2000; Mégnin and Romanowicz, 2000] and the increase of their wavelength [Mégnin and Romanowicz, 2000; Su and Dziewonski, 1991; Li and Romanowicz, 1996]. These observations suggest the presence of broad seismic velocity anomalies in the deep mantle, also generally observed by different tomographic models [Grand *et al.*, 1997; van der Hilst *et al.*, 1997; Masters *et al.*, 2000; Mégnin and Romanowicz, 2000] and inferred by normal mode and free-air gravity data [Ishii and Tromp, 1999]. The large size of these anomalies is inconsistent with purely thermal convection and rather suggests the existence of chemical heterogeneities in the lowermost mantle. Seismic tomography provides supplementary informations on the nature of deep mantle heterogeneities by using ratios and relative variations of seismic velocities for real and theoretical body waves such as: (i) The ratio R of the relative variations of S-wave to P-wave velocities. Horizontally averaged R profiles show that R increases below 2000 km depth from 1.7 to values greater than 2.7 near the Core-Mantle Boundary (CMB) [Masters *et al.*, 2000; Saltzer *et al.*, 2001; Romanowicz, 2001]. Such high R cannot be explained by temperature differences alone but require the presence of compositional heterogeneities [Masters *et al.*, 2000] and possibly anelasticity [Karato and Karki, 2001]. (ii) The anticorrelation between bulk sound speed and shear wave velocity anomalies in the lowermost mantle is also derived from several tomographic models [Kennett *et al.*, 1998; Masters *et al.*, 2000; Saltzer *et al.*, 2001; Antolik *et al.*, 2003], and suggests the presence of chemical density heterogeneities. While there is a general agreement on the RMS profiles and on the presence of broad seismic velocity anomalies in the lowermost mantle, high R values and the anticorrelation between V_S and V_ϕ are not commonly shown by tomographic models (see [Masters *et al.*, 2000] for a review). However, these differences are not necessarily contradictory. Indeed, Saltzer *et al.* [2001] found that indicators of compositional heterogeneity (i.e., $R > 2.7$ and anticorrelation between V_ϕ and V_S) can be hidden in horizontally averaged profiles because of their lateral variability. They found that areas away from slab regions present both $R > 2.5$ and anticorrelation between V_S and V_ϕ , while areas near slab regions have $R < 2.5$ and no anticorrelation. This could explain, among other things, the apparent discrepancies

between different tomographic models, concerning R profiles and the presence of anticorrelation.

Tomographic models thus strongly suggest the existence of compositional heterogeneity in the deep mantle, which is also required by geochemical considerations. The large differences in trace elements and noble gases between Mid Ocean Ridge Basalts (MORBs) and Ocean Island Basalts (OIBs) require the presence of at least two distinct reservoirs for billions of years (see [Hofmann, 1997] for a review). Laboratory experiments (e.g., [Lebars and Davaille, 2002] and references therein) and 2D-3D numerical simulations (e.g., [Tackley, 2002; Samuel and Farnetani, 2003] and references therein) have investigated the long term stability and stirring of chemically denser material. A major conclusion is that even a small excess of chemical density ($\sim 1\%$) profoundly affects the nature of mantle convection. Under certain conditions, thermochemical convection provides a way to maintain separated reservoirs for billions of years. Assuming a relatively undegassed denser material, [Samuel and Farnetani, 2003] show that thermochemical convection can explain the observed helium ratios for MORB and OIB.

It is therefore difficult to interpret several geophysical and geochemical observations without the presence of chemically denser material in the lowermost mantle. Previous studies investigated possible mechanisms that could generate a chemical density excess, $\Delta\rho_\chi$, in the lower mantle. Considering a lower mantle assemblage of perovskite (Fe,Mg)SiO₃ and magnesiowüstite (Fe,Mg)O, Forte and Mitrovica [2001] and more recently Deschamps and Trampert [2003] suggested that $\Delta\rho_\chi$ could be due to variations of the iron and silica content as proposed by Kellogg *et al.* [1999], while Sidorin and Gurnis [1998] claimed for the additional presence of SiO₂ stishovite to satisfy their geodynamical and seismological constraints. Furthermore, Karato and Karki [2001] concluded that variations in Si and Fe content alone cannot explain values of $R > 2.7$, and proposed that the presence of Ca-perovskite could satisfy this constraint. It is hard to directly compare these results, because they ensue from different reasonings: for instance the chemical density contrast considered by [Sidorin and Gurnis, 1998] is much higher than the one required by [Forte and Mitrovica, 2001]. Anelasticity is neglected in [Sidorin and Gurnis, 1998] and [Deschamps and Trampert, 2003], contrary to [Karato and Karki, 2001] and [Forte and Mitrovica, 2001]. Finally, the constraints considered by these studies for the composition of the chemically denser material differ widely.

In this paper, we focus on the lower mantle and we investigate the effect of compositional heterogeneities on seismological models and observations. Similar to [Forte and Mitrovica, 2001] we assume that the lower mantle is an assemblage of the main perovskite and magnesiowüstite phases

and do not consider the effect of less abundant components such as Ca and Al. We also assume that the composition of the heterogeneous denser material in the lowermost mantle is due to variations in Fe, Mg and Si content, relative to a pyrolytic lower mantle. First, we model thermochemical convection from 2 Gy ago to present day time, in order to: (i) constrain the chemical density excess $\Delta\rho_\chi$ required for the material to remain stable, (ii) obtain the temperature field, the geometry and distribution of the chemical heterogeneities. Second, we calculate the seismic velocity anomalies of P-wave, S-wave and bulk sound for a wide range of compositions. Third, we use geodynamical and seismological considerations to constrain the composition of the dense material. Finally, we assign the calculated composition to the dense material in our geodynamical model. Our predicted seismic velocity anomalies, R profiles and distributions and anticorrelation are then compared to seismological observations.

1.1. Convection model

We use the numerical code for solid state convection STAG3D by P. Tackley, which has been described in detail in [Tackley, 2002] and references therein. The code, in cartesian geometry, solves the equations of conservation of mass, conservation of momentum, conservation of energy, and the advection of a compositional field. In our two dimensional convection calculations, we use 25 active tracer particles per cell to model the presence of chemically denser material. The code allows vertical compressibility, therefore the density ρ , the thermal expansion α and the thermal conductivity k are depth dependent, as described in the next section.

The characteristic scales used to normalize the governing equations are the mantle depth $D=2890$ km, the surface density ρ_0 , the superadiabatic temperature drop $\Delta T=2500$ K. A thermal diffusion timescale is used: D^2/κ where $\kappa = k/\rho C_P$ is the thermal diffusivity, the specific heat $C_P=1200$ J kg⁻¹ K⁻¹ is assumed constant. The internal heating is scaled over $\rho D^2/k\Delta T$. Three non dimensional numbers appear from the normalization of conservation equations: the surface dissipation number

$$Di_0 = \frac{\alpha_0 g D}{C_P}, \quad (1)$$

the Rayleigh number based on surface parameters:

$$Ra = \frac{\rho_0 \alpha_0 \Delta T g D^3}{\kappa_0 \eta_r}, \quad (2)$$

the surface buoyancy number:

$$B = \frac{\Delta\rho_\chi}{\rho_0 \alpha_0 \Delta T}, \quad (3)$$

where α_0 is the surface thermal expansion, the reference viscosity $\eta_r = 1.13 \cdot 10^{22}$ Pa s, the gravitational acceleration $g=10$ m s⁻². $\Delta\rho_\chi$ is the chemical density excess with respect to the reference density. Therefore, temperature and compositional effect on density ρ are calculated with the linearized equation of state: $\rho = \rho_0(1 - \alpha(T - T_0) + \Delta\rho_\chi/\rho_0\chi)$.

Similar to [Samuel and Farnetani, 2003], homogeneous internal heating H is linked to concentrations of ²³⁸U, ²³⁵U, ²³²Th and ⁴⁰K that vary as a function of time because of radioactive decay (using values of radioactive decay constants listed in [Turcotte and Schubert, 1982]). This yield values of H from 31 at $t=2$ Gy B.P. to 19, corresponding to actual concentrations of U=17 ppb (with ²³⁸U/²³⁵U=135.88) ²³²Th=65 ppb and ⁴⁰K=25 ppb (using the heat production rates for ²³⁸U, ²³⁵U, ²³²Th and ⁴⁰K given in [Turcotte and Schubert, 1982]).

Our model domain is constituted of 768×128 square cells providing the resolution of 22.6 km/cell. At the top and bottom surfaces the temperature is constant and we impose zero vertical velocity and horizontal free slip. At the sidewalls, periodic boundary conditions for temperature and velocity are imposed.

1.2. Thermodynamical model and parameters

1.2.1. Thermodynamical model. The code uses a thermodynamical model for depth dependent parameters (temperature, density and thermal expansion). The depth dependence of temperature is assumed adiabatic:

$$\frac{\partial T'}{\partial z'} = -DiT', \quad (4)$$

where the primes denote non-dimensional values. Density varies with depth according to the Adams-Williamson equation of state:

$$\frac{\partial \rho'}{\partial z'} = -\frac{Di}{\gamma} \rho', \quad (5)$$

$\gamma = \alpha K_S/\rho C_P$ is the thermodynamical Grüneisen parameter, with the assumption that $\gamma\rho$ is constant. K_S is the adiabatic bulk modulus.

Thermal expansion α varies according to the semi-empirical relation [Anderson et al., 1992]:

$$\alpha = \alpha_0 \exp\left[-\frac{\delta_{T_0}}{n} \left(1 - \left(\frac{\rho_0}{\rho}\right)^n\right)\right], \quad (6)$$

with $\delta_{T_0} = -\left(\frac{1}{K_T}\right)\left(\frac{\partial K_T}{\partial T}\right)_P$ the isothermal Anderson Grüneisen parameter at ambient conditions, n is a constant equal to 1.4, and K_T is the isothermal bulk modulus.

1.2.2. Thermodynamical parameters. Our objective is to investigate the effect of the presence of chemically denser material on seismic velocity anomalies in the lowermost mantle. For simplicity, we do not consider phase changes and variable viscosity. Since we are interested in lower mantle compositions, we consider only lower mantle assemblages with two phases: perovskite (Fe,Mg)SiO₃ and magnesiowüstite (Fe,Mg)O. The third component, CaSiO₃ perovskite, has elastic parameters close to (Fe,Mg)SiO₃ perovskite and is thus neglected, which appears to be a reasonable assumption as shown by [Deschamps and Trampert, 2003]. Therefore, the values of the parameters chosen for our convection calculations must be consistent with respect to this assemblage. Assuming a pyrolitic composition for the reference mantle, the density of the assemblage of perovskite and magnesiowüstite at room conditions is $\rho_0=4160 \text{ kg m}^{-3}$ (using relations given in Table 1).

Surface values of ρ_0 , γ_0 , δ_{T_0} , and α_0 , listed in Table 2, were evaluated assuming an assemblage of perovskite and magnesiowüstite. We take $\delta_{T_0}=4.6$ for the mantle composition which falls well within $\delta_{T_0}^{pv}=4.1$ [Gillet *et al.*, 2000] and $\delta_{T_0}^{mw}=6$ [Chopelas and Boehler, 1992] at ambient conditions. $\gamma_0=1.33$ was estimated by doing a Voigt average of $\gamma_0^{pv}=1.31$ and $\gamma_0^{mw}=1.41$ [Jackson, 1998] with a volumic proportion of 80% perovskite. The thermal expansion coefficient at ambient conditions for perovskite ranges between $\sim 2 \cdot 10^{-5} \text{ K}^{-1}$ and $\sim 4 \cdot 10^{-5} \text{ K}^{-1}$, depending on its iron content [Karki and Stixrude, 1999], while for magnesiowüstite studies seem to agree for a value close to $3 \cdot 10^{-5} \text{ K}^{-1}$ [Hama and Suito, 1999], therefore we use $\alpha_0=2.7 \cdot 10^{-5} \text{ K}^{-1}$.

Using Equations 4, 5 and 6, we obtain $\rho=5620 \text{ kg m}^{-3}$ at the Core-Mantle Boundary (CMB), which is in good agreement with PREM [Dziewonski and Anderson, 1981]. The calculated thermal expansion coefficient $\alpha=0.9 \cdot 10^{-5} \text{ K}^{-1}$ at the CMB is also consistent with high pressure experiments [Chopelas and Boehler, 1992]. The temperature at the CMB $T_b=3470 \text{ K}$ is about 100 K lower than a previous estimation by [Brown and Shankland, 1981]. This choice of physical and thermodynamical parameters leads to a surface $Ra = 10^7$.

2. CALCULATION OF SEISMIC VELOCITIES

2.1. Formalism

In order to compare our thermochemical model with seismological observables, we calculate the seismic velocities for a wide range of mineralogical compositions combined with the temperature field obtained with the convection code. Making the assumption that the lower mantle is seismically isotropic [Meade *et al.*, 1995], the seismic velocities of P-wave and S-wave are respectively:

$$V_P = \left(\frac{K_S + \frac{4}{3}\mu}{\rho} \right)^{1/2} \quad V_S = \left(\frac{\mu}{\rho} \right)^{1/2}, \quad (7)$$

where K_S is the adiabatic bulk modulus and μ the shear modulus. Another parameter commonly used in tomographic models is the theoretical bulk sound speed:

$$V_\Phi = \left(V_P^2 - \frac{4}{3}V_S^2 \right)^{1/2} = \left(\frac{K_S}{\rho} \right)^{1/2}. \quad (8)$$

K_S , μ and ρ depend on temperature, pressure and composition. For our mineralogical model composed of perovskite (Fe,Mg)SiO₃ and magnesiowüstite (Fe,Mg)O, the composition is defined by: the iron molar ratio $xFe = nFe/(nFe + nMg) = 1 - xMg$, the silica molar ratio $xSi = nSi/(nFe + nMg)$, and the iron-magnesium partition coefficient:

$$KFe = \frac{(xFe/xMg)_{mw}}{(xFe/xMg)_{pv}}. \quad (9)$$

For a given xSi , xFe composition and KFe we calculate $K_S^{P,T}$, $\mu^{P,T}$ and $\rho^{P,T}$ for each of the two phases considered. We can then derive $V_P(T, P)$, $V_S(T, P)$ and $V_\Phi(T, P)$ in our mantle domain, proceeding as follows:

We consider a third order Birch-Murnaghan finite strain formalism [Birch, 1952], for which the pressure along an adiabat writes:

$$P = \frac{3}{2}K_S^{P_0, T_S} \left[\left(\frac{\rho^{P, T_S}}{\rho^{P_0, T_S}} \right)^{(7/3)} - \left(\frac{\rho^{P, T_S}}{\rho^{P_0, T_S}} \right)^{(5/3)} \right] \left\{ 1 + \frac{3}{4}(K'_S - 4) \left[\left(\frac{\rho^{P, T_S}}{\rho^{P_0, T_S}} \right)^{(2/3)} - 1 \right] \right\}, \quad (10)$$

where $K'_S = (\partial K_S / \partial P)_{P=P_0}$, T_{S0} is the temperature at the top of the adiabat considered (Figure 1a), and ρ^{P_0, T_S} is approximated by:

$$\rho^{P_0, T_S} = \rho^{P_0, T_0} [1 - (T_S - T_0)\alpha^{P_0, T_0}]. \quad (11)$$

For each phase ρ^{P_0, T_0} the density at ambient conditions $T_0=300 \text{ K}$ and $P_0 \sim 0 \text{ Pa}$, is calculated using the molar mass and molar volume of each component (Fe, Si, Mg, O). This yields the relations given in [Wang and Weidner, 1996] (see Table 1). Thus, using Equation 10, we calculate for each phase, ρ^{P, T_S} the density along the adiabat.

Following [Stacey and Davis, 2004], we calculate $K_S^{P,T}$ for perovskite and magnesiowüstite at pressure P and temperature T by differentiation of Equation 10 and by considering a linear dependence of K_S with temperature:

$$K_S^{P,T} = P \frac{-a(5/3)\Gamma^{5/3} + b(7/3)\Gamma^{7/3} - 3c\Gamma^3}{-a\Gamma^{5/3} + b\Gamma^{7/3} - c\Gamma^3} + \left(\frac{\partial K_S}{\partial T} \right)_P (T - T_S), \quad (12)$$

where $\Gamma = \rho^{P,T_s}/\rho^{P_0,T_s}$, $a = -2(K' - 4) + (8/3)$, $b = -4(K' - 4) + (8/3)$ and $c = b - a$.

The next step before calculating $\rho^{P,T}$ is to express $\alpha^{P,T}$, the thermal expansion coefficient at P and T . We make the reasonable assumption that T is above the Debye temperature and we use the relationship:

$$\gamma^{P,T} \rho^{P,T} = \gamma^{P_0,T_{S_0}} \rho^{P_0,T_{S_0}}, \quad (13)$$

with

$$\gamma = \frac{\alpha K_S}{\rho C_P}. \quad (14)$$

Combining Equations 13 and 14 gives:

$$\alpha^{P,T} = \frac{\gamma^{P_0,T_{S_0}} \rho^{P_0,T_{S_0}} C_P^P}{K_S^{P,T}}, \quad (15)$$

where we consider a pressure dependence for the specific heat C_P (see appendix B). Then we calculate $\rho^{P,T}$ using the equivalent form of Equation 11.

The pressure (or volume) dependence of shear modulus is then evaluated using the relationship [Davies, 1974]:

$$\mu^{P,T_0} = \left(\frac{\rho^{P,T_0}}{\rho^{P_0,T_0}} \right)^{5/3} \left\{ \mu^{P_0,T_0} + \frac{1}{2} \left[5\mu^{P_0,T_0} - 3 \left(\frac{\partial \mu}{\partial P} \right)_T K^{P_0,T_0} \right] \right\} \left[1 - \left(\frac{\rho^{P,T_0}}{\rho^{P_0,T_0}} \right)^{2/3} \right], \quad (16)$$

and its temperature dependence is expressed as:

$$\mu^{P,T} = \mu^{P,T_0} + \left(\frac{\partial \mu}{\partial T} \right)_P (T - T_0). \quad (17)$$

Finally we obtain $\rho^{P,T}$, $K_S^{P,T}$ and $\mu^{P,T}$ for pure perovskite and magnesiowüstite. We next calculate $\varphi^{P,T}$, the volumic proportion of perovskite in the assemblage of a given composition. The elastic coefficients for the assemblage are obtained by doing a Voigt-Reuss-Hill average [Watt et al., 1976], while the density of the assemblage is calculated by doing a Voigt average:

$$\rho_a^{P,T} = \varphi^{P,T} \rho_{pv}^{P,T} + (1 - \varphi^{P,T}) \rho_{mw}^{P,T}. \quad (18)$$

Using Equations 7 and 8, we obtain the P-wave and S-wave velocities as well as the bulk sound speed for the assemblage of perovskite and magnesiowüstite.

Note that since we do not take into account phase changes and consider only lower mantle phases, we take pressure from PREM [Dziewonski and Anderson, 1981] instead of computing the lithostatic pressure with our densities, which would have biased the results.

The isothermal bulk and shear modulus for Mg-perovskite and periclase and their derivatives with respect to T and P we use for the calculations detailed above are given in Table 3. We have chosen to use these values derived from molecular dynamic calculations [Matsui, 2000] because they are auto-coherent and compatible with recent experimental results. We made however an exception for the value of $\partial \mu / \partial T = -0.019$ GPa K⁻¹ for perovskite which appears too low compared with values proposed by other studies, that generally range between -0.027 GPa K⁻¹ and -0.029 GPa K⁻¹ [Duffy and Anderson, 1989; Sinelnikov et al., 1998]. Thus, we use $\partial \mu / \partial T = -0.024$ GPa K⁻¹, the average of the extreme values. Since seismic waves propagation is adiabatic, we convert the isothermal values for bulk modulus (Table 3) to the adiabatic case (see appendix A). For shear modulus, there is no significant difference between adiabatic and isothermal case [Poirier, 1991].

In these calculations, the influence of xFe on the elastic coefficients is taken into account for Mg_{*x*}Fe_{*x*}SiO₃ perovskite and for Mg_{*x*}Fe_{*x*}O magnesiowüstite (Table 1). Experiments have shown that the bulk modulus of perovskite [Yeganeh-Haeri, 1994] is not affected by the presence of iron. The influence of iron on the shear modulus of perovskite is expected to be small (see [Wang and Weidner, 1996] and references therein), however there are no confirmation available from high pressure and temperature experiments.

2.2. The reference mantle

Seismic tomography displays velocity *anomalies* with respect to a reference model, which is often PREM, or with respect to the average velocity. Therefore, we need to choose a reference model in order to express our seismic velocities in terms of velocity anomalies. The assumed pyrolitic composition for our reference mantle is defined by $xSi = 0.68$ and $xFe = 0.11$. Although KFe is pressure dependent its value above 40 GPa (i.e., below ~ 1000 km depth) seems to be constant and about 3.5 [Guyot et al., 1988]. Therefore, we assume $KFe = 3.5$ through all our reference mantle. The reference temperature profile (shown in Figure 1a) is assumed to be adiabatic with a top adiabat at 1700 K, plus

thermal boundary layers ~ 90 km thick at the top and bottom. The calculated reference density (Figure 1b) gives a very good fit to PREM in the lower mantle. As expected, the fit is poor in the upper mantle since we have considered only lower mantle phases. Figure 1c shows depth profiles of thermal expansion coefficient for pure perovskite, pure magnesiowüstite and for the assemblage. At ambient conditions, the thermal expansion coefficient for perovskite and for magnesiowüstite are respectively $2.6 \cdot 10^{-5} \text{ K}^{-1}$ and $4.1 \cdot 10^{-5} \text{ K}^{-1}$. Such values are higher than experimental estimates for Mg-perovskite [Fiquet *et al.*, 2000; Gillet *et al.*, 2000] and magnesiowüstite (see [Hama and Suito, 1999] and references therein). However, these experiments have been performed on pure Mg-perovskite and periclase, while our results include the presence of iron in both phases. As pointed out by [Karki and Stixrude, 1999], measurements on Fe-bearing samples yield much higher values of thermal expansion at ambient conditions. The calculated volumic proportion of perovskite in the assemblage at ambient conditions is $\varphi^{P_0, T_0} = 82\%$, providing a thermal expansion coefficient for the assemblage $\alpha^{P_0, T_0} = 2.8 \cdot 10^{-5} \text{ K}^{-1}$. At high pressure and temperature ($P=135$ GPa and $T=3450$ K) α is $1.0 \cdot 10^{-5} \text{ K}^{-1}$ for magnesiowüstite and $0.94 \cdot 10^{-5} \text{ K}^{-1}$ for perovskite, which compare well with experiments on Mg-perovskite [Gillet *et al.*, 2000] and MgO [Chopelas and Boehler, 1992].

3. RESULTS

3.1. Behavior of the chemically denser material

We start the calculations at $t_0=2$ Gy before present, which corresponds to the mean age of continental crust, and assume that the dense layer represents 25% of the whole mantle volume. We choose this ‘initial’ time in order to avoid the modeling of continental crust extraction.

Similar to [Tackley, 2002], our initial condition for temperature was obtained by running the calculations with the dense layer until reaching a thermal equilibrium. We affect a large value of the buoyancy number ($B=0.5$) in order to keep the denser material in the bottom of the lower mantle with no topography. At t_0 , the surface buoyancy number B is set to 0.25, which corresponds to a chemical density contrast $\Delta\rho_\chi/\rho_0=1.7\%$.

Plate 1a shows the non dimensional potential temperature field (i.e., the temperature without the adiabatic gradient) obtained after running our calculation for 2 Gy after t_0 . The presence of relatively small chemical density excess $\Delta\rho_\chi/\rho=1.7\%$ greatly influences the nature of convection. The hot denser material develops a topography and is not continuous, being deflected by cold plumes (e.g. see Plates 1a and 1b at $x/D=0.20$ and $x/D=5.5$). Therefore we use the term ‘dense material’ rather than ‘dense layer’. The chemical density

excess prevents the dense material from a complete mixing with the overlying mantle, however it is not high enough to produce a flat interface. The interface is a thermal boundary layer across which the temperature jump ranges between 300 and 800 K, as shown also in the horizontally averaged temperature profile (Figure 1a). Hot plumes are generated from domes of dense material, the height of the domes is on average 500 ± 250 km and can extend to a depth of 1500 km (e.g. see Plate 1b at $x/D=5.0$). The volume of the dense material accumulated at the bottom of the lower mantle is about 15 % of the whole mantle volume, therefore 40 % of its initial volume has been brought in the overlying mantle, where stirring is efficient [Farnetani and Samuel, 2003; Samuel and Farnetani, 2003]. Filaments of heterogeneous dense material (i.e., $\chi > 0$) stretched by the convective stirring are easily visible in Plate 1b.

Finally, the value of $\Delta\rho_\chi/\rho=1.7\%$ allows a significant amount of dense material to remain stable at present day time, with a topography. Indeed, if $\Delta\rho_\chi/\rho$ is lower than 1.7%, the dense material cannot remain stable and will be rapidly mixed with the overlying mantle, while if $\Delta\rho_\chi/\rho$ is too high, the dense material will form a flat interface, which is not observed by seismology. We remark that variable viscosity would help to stabilize the dense material [Tackley, 2002; Samuel and Farnetani, 2003]. Therefore, we can reasonably consider that $\Delta\rho_\chi/\rho$ required to give a stable dense material with a topography ranges between 1% and 2% and perhaps less, depending on the distribution of heat producing elements in the mantle.

In our model, the homogeneous internal heating rate is linked to the time-decreasing concentrations in heat producing elements (due to radioactive decay, see section 1.1). Therefore the term ‘present day’ indicates a time for which the concentrations of heat producing elements in our model corresponds to present-day estimates of U, Th and K mantle content, based on chondritic models (e.g., [McDonough and Sun, 1995]). We should point out that the relatively high value of the constant viscosity chosen here yields the dimensional time based on a convective time scale about 6 times smaller than the one based on the diffusive time scale. Nevertheless, even when choosing a convective time scale, we checked that the dense material could survive at least 2 Gy after our initial condition. The reason for this is that the set of parameter chosen for the convection model yields a quasi-dynamic equilibrium of the thermochemical system and the entrainment of dense material by thermal plumes is relatively low. However, when viscosity is temperature dependent, one should expect a higher entrainment [Zhong and Hager, 2003]. This would therefore require a somewhat higher value of the chemical density contrast in order for the dense material to survive for 2 Gy.

3.2. Constraints on the composition of the dense material

In the following, we consider two mineralogical end members: (i) the reference mantle, assumed to have a pyrolitic composition, (ii) the denser material, whose mineralogical composition has to be constrained. Our approach is to use seismological models and observations as well as geodynamical considerations, to constrain the composition of the dense material. Our strategy is to calculate the seismic velocity anomalies with respect to our reference mantle for a large range of mineralogical compositions, and then to use seismology and geodynamics to constrain the composition of the dense material. For seismological constraints, we especially focus on the anticorrelation between shear wave velocity and bulk sound speed anomalies, associated with slow shear wave velocities. The second type of constraint arises from geodynamical considerations on the stability of the dense material. As previously mentioned, we can reasonably consider that $\Delta\rho_\chi/\rho$ (at ambient conditions) required to produce a stable dense material with a dynamical topography is between 1% and 2%.

Therefore, we require the following constraints to be satisfied simultaneously:

- (1) $d\ln V_\phi/d\ln V_S < 0$ associated with $d\ln V_S < 0$.
- (2) $\Delta\rho_\chi/\rho = 1 - 2\%$.

The calculation of seismic velocity anomalies is first performed at a pressure of 100 GPa, corresponding to ~ 2200 km since at this depth: the dense material in our numerical model starts to appear, and seismological observations indicate the existence of heterogeneity. According to our reference temperature profile (Figure 1a), the temperature at $P=100$ GPa is 2200 K. Following the approach detailed in section 2.1, we calculate the seismic velocity anomalies for a large range of xFe and xSi molar ratios. Plate 2 shows the results for two cases, where we vary the temperature contrast δT between the reference mantle and the hot dense material, and/or the iron-magnesium partition coefficient KFe between magnesiowüstite and perovskite for the dense material. In the first case (Plate 2a) $\delta T=400$ K and $KFe=3.5$ for the dense material. The blue curve corresponds to $d\ln V_S=0$ while the red curve corresponds to $d\ln V_\phi=0$. Above the blue and the red curves, $d\ln V_S$ and $d\ln V_\phi$ are negative, respectively. Therefore, areas in dark and light grey correspond to compositions that would give an anticorrelation between bulk sound speed and shear wave velocity. Moreover, the light grey area corresponds to compositions for which anticorrelation between V_S and V_ϕ is associated with slow shear wave velocity. This corresponds to our first constraint. The composition of the dense material should therefore lie within the light grey area. We can further constrain the composition by taking into account

our geodynamical considerations (constraint 2). Isocontours of chemical density excess at ambient temperature are represented by the black lines in Plate 2: $\Delta\rho_\chi/\rho=0\%$ (i.e., no chemical density excess), 1%, 2% and 4%, while the green line is a specific isocontour $\Delta\rho_\chi/\rho = 1.7\%$ corresponding to our geodynamical model. $\Delta\rho_\chi/\rho$ were obtained by computing the densities at ambient temperature for the reference pyrolitic mantle and for a wide range of xFe and xSi compositions, as detailed in section 2.1 but at $T=300$ K. The normalized density difference between the reference mantle and composition corresponding to various xSi and xFe thus represents $\Delta\rho_\chi/\rho$. The compositions which satisfy both geodynamical and seismological considerations lie within the orange area since they satisfy simultaneously constraints 1 and 2. In agreement with previous work [Kellogg *et al.*, 1999] the dense material has to be enriched in both iron and silica with respect to a pyrolitic composition (represented by the triangle in Plate 2). For $\Delta\rho_\chi/\rho = 1.7\%$, the composition which differs the least from the reference pyrolitic composition is defined by the intersection of the green line ($\Delta\rho_\chi/\rho = 1.7\%$) and the red line ($d\ln V_\phi=0$).

We find $xFe = 0.17$ and $xSi = 0.81$ when $\delta T=400$ K and $KFe=3.5$ for the dense material (Plate 2a). For a higher temperature contrast between the reference mantle and the hot dense material $\delta T=800$ K, (Plate 2b) a greater increase of xSi is required, while xFe remains unchanged with respect to the previous case. However, such high temperature contrast is inconsistent with the excess temperature of mantle plumes [Farnetani, 1997]. We also investigate the influence of a lower KFe for the dense material, which could be due to the presence of a small amount of aluminum in perovskite at high pressure [Andrault, 2001]. Al-perovskite is not explicitly taken into account in our calculations, since we neglect the possible effect of Al on V_0 , K and μ for perovskite. However, this simplification is probably reasonable since the amount of Al-perovskite necessary to decrease KFe is relatively low [Andrault, 2001]. We find no significant differences in silica and iron content with respect to the cases where $KFe=3.5$. Table 4 summarizes the main results presented in Plates 2a-b.

Calculations have also been conducted at higher (i.e., up to 135 GPa) and lower (i.e., 25 GPa) pressures. In either case we find that the results described above remain valid. Similarly, we investigated the effect of the reference mantle temperature and find that even a wide range of temperatures (1800-3000 K) does not affect significantly our results. Therefore, for the most plausible case, $\delta T=400$ K, our preferred compositions for the dense material (i.e., those which differ the least from the reference pyrolitic mantle) range between 0.77 and 0.81 for xSi , and between 0.14 and 0.17 for xFe , depending on the chemical density contrast $\Delta\rho_\chi$ required (see Table 4).

3.3. Comparison with seismological observables

3.3.1. Check of models coherency. From further considerations, we fix the composition of the dense material to $xSi=0.81$, $xFe=0.17$, and $KFe=3.5$, thus for $\Delta\rho_\chi/\rho = 1.7\%$. Since we use two different formalisms for the geodynamical model (Equations 5 and 6) and for the post-processing calculation of seismic velocities (see section 2.1), it is important to check that our preferred composition produces the same critical quantities obtained by the numerical convection code. From a geodynamical point of view, the critical quantity for the stability of the dense material, for a given temperature field, is the effective buoyancy number: $B_{eff} = \Delta\rho_\chi/(\rho\alpha(T-T_0))$. In Figure 2a we compare the horizontally averaged B_{eff} obtained from STAG3D with B_{eff} from our post-processing calculations, while in Figure 2b we compare the horizontally averaged chemical density contrast $\Delta\rho_\chi/\rho_0$ (without the effect of temperature) given by STAG3D with $\Delta\rho_\chi/\rho_0$ from our post-processing calculations. In both figures, the small differences indicate a satisfactory coherence between the *a priori* thermodynamical model used in STAG3D and the post-processing calculations.

3.3.2. Seismic velocity anomalies. We calculate seismic velocity anomalies with respect to our reference using the temperature and the compositional fields shown in Plates 1a and 1b. Values of xSi and xFe are linearly linked to the value of the compositional field: $\chi=0$ corresponds to a pyrolytic composition while $\chi=1$ corresponds to $xSi = 0.81$ and $xFe = 0.17$. The obtained seismic velocity anomaly field for bulk sound (Plate 1c) and shear wave (Plate 1d) have globally a comparable shape, mainly induced by the temperature field. The amplitude of the anomalies for shear wave ranges between $\pm 4\%$ while for bulk sound speed, less sensitive to temperature heterogeneity, the anomalies range between $\pm 1\%$. Seismic velocity anomalies for P-waves (not shown) range between $\pm 1.7\%$, and have a similar shape to $\ln V_S$ and $\ln V_\phi$ fields. The calculated velocity anomalies compare fairly well with seismic tomography of the lower mantle (e.g., [Mégnin and Romanowicz, 2000]). Another important feature in good agreement with local seismic studies of the lower mantle [Bréger *et al.*, 2001] is the sharp lateral variation in seismic velocity, induced by the coexistence of hotter, denser material with cold plumes. We remark that strong lateral variations in temperatures are a specific feature of thermochemical convection and cannot be generated by purely thermal convection models, for which the hot buoyant material is free to rise at shallower depths.

Although seismic velocity anomaly fields for bulk sound and shear wave have globally a comparable shape, several differences can be observed (e.g. compare Figures 1c and

1d at $x/D=0.25$ and $z/D=0-0.25$), where $\ln V_S$ is negative while $\ln V_\phi$ is positive. These differences produce areas of anticorrelation between V_S and V_ϕ (Plate 1e). The composition chosen for the dense material, combined with our temperature field, is responsible for this anticorrelation associated with slow shear wave velocities. We remark that these areas are not located everywhere inside the dense material because the temperature contrast δT between the two materials is too high to produce any anticorrelation (see Plate 2). Instead, anticorrelation areas are mostly located at the interface between the hot dense material and the overlying pyrolytic mantle where temperature (and compositional) gradients are strong. Moreover, anticorrelation areas are mainly associated with upwelling regions, while there is almost no anticorrelation in downwelling regions. This is in remarkably good agreement with recent observation by Saltzer *et al.* [2001].

The amplitudes of our calculated seismic velocity anomalies are higher than those displayed by tomographic models, mainly for two reasons: First, our model resolution of 22.6 km is much higher than the resolution of tomographic models in the lower mantle. Thus, we are able to display small structures that cannot be imaged by seismic tomography. We altered the resolution of our model from 22.6 km to 180 km using a filter (see appendix C) and we find that the amplitudes of seismic velocity anomalies are reduced to $\pm 3.5\%$ for shear wave, $\pm 1\%$ for compressional waves and $\pm 0.5\%$ for bulk sound speed. Note that even with filtering, all the results described above remain unchanged. The second reason is that tomographic models underestimate the amplitude of seismic velocity anomalies, sometimes by a factor 3, as a result of damping [Bréger *et al.*, 1998].

3.3.3. RMS seismic velocity profiles. A common feature of tomographic models is the increase of the Root Mean Square (RMS) seismic velocity anomaly below ~ 2000 km [Masters *et al.*, 2000; Mégnin and Romanowicz, 2000]. Since RMS seismic velocity gives a measure of the lateral variations of seismic velocity anomalies, the observations suggest an increase of mantle lateral heterogeneity below 2000 km. Figure 3a shows the RMS seismic velocity anomalies for shear, compressional and for bulk sound. Note that we purposely exclude values corresponding to depth greater than 2800 km because our constant temperature boundary condition at the bottom hinders lateral temperature variations below this depth. All calculated RMS profiles show an increase below ~ 2000 km depth, in good agreement with tomographic studies. This is due to the topography formed by the dense hotter material in the lowermost mantle. Again, we note that purely thermal convection models are unable to reproduce the observed RMS profiles.

3.3.4. The ratio R in the lower mantle. Supplementary information about mantle chemical heterogeneity can be provided by the ratio R of shear to compressional velocity anomaly:

$$R = \frac{d \ln V_S}{d \ln V_P}. \quad (19)$$

It has been argued that above a critical value of $R=2.5-2.7$ seismic velocity anomalies cannot be explained by temperature differences alone, but point out chemical density differences [Masters *et al.*, 2000; Karato and Karki, 2001]. Global joint tomographic models [Robertson and Woodhouse, 1996; Masters *et al.*, 2000], have shown that, on average, R increases with depth from about 1.5-1.7 at 1000 km, to values sometimes greater than 3 near the core-mantle boundary, with R becoming greater than 2.5 at approximately 2000 km depth. Saltzer *et al.* [2001] have shown that the R ratio has a lateral variability, especially in the lowermost mantle, with areas where R is greater than 2.5 and others where R is lower than 2, depending on the lateral position. Our calculated horizontally averaged R profile is about 1.5 at 1000 km and increases with depth to 2.2 at 2800 km depth (Figure 3b). However, R has a large lateral variability as clearly visible in Plate 1f which displays areas with $R > 2.7$. These areas match fairly well areas of anticorrelation between V_ϕ and V_S (Plate 1e), emphasizing that these two features are closely related to each other. The maximum R values (Figure 3b) show that the horizontally averaged R profile hides lateral variations of $R > 2.7$, which can instead reach values up to 5. The good agreement of our results with tomographic studies, in particular [Saltzer *et al.*, 2001], strongly supports the idea that chemical heterogeneity varies laterally as well as the anticorrelation between V_S and V_ϕ . This may explain the reason why some tomographic models find relatively low R (< 2.5) [Kennett *et al.*, 1998], depending on the seismic area covered.

3.3.5. Effect of anelasticity. Anelasticity as well as anharmonicity may play an important role when one tries to explain values of R greater than 2.7 [Karato, 1993; Karato and Karki, 2001]. We thus investigated the effect of anelasticity on our results, following Karato & Karki's approach [Karato and Karki, 2001]. Details of calculation can be found in appendix D. As shown in Figure 3b, when anelastic effects are taken into account, the averaged R profile is higher, leading to values that range between 2.7 and 4 below 2000 km, in agreement with [Karato and Karki, 2001]. However, anelasticity as well as the presence of Ca variations do not seem to be necessary to explain values of R greater than 2.7, contrary to the conclusions of [Karato and Karki, 2001]. This discrepancy between our results and the study of Karato and Karki [2001] can be explained by the higher lateral tempera-

ture variations they have considered in the lowermost mantle. It is important to remark that considering anelasticity does not modify our results on the composition of the dense material. This can easily be seen in Plate 2 where we determine our preferred composition for the dense material as the intersection between the two isocontours $\Delta\rho_\chi/\rho = 1.7\%$ and $d \ln V_\phi = 0$. Since anelasticity affects only S-waves but not P-wave or bulk sound speed, it will not change the position of the two isocontours $\Delta\rho_\chi/\rho = 1.7\%$ and $d \ln V_\phi = 0$ in Plate 2 and thus the composition of the dense material according to our criteria.

3.3.6. Differences between our reference model and PREM. Although it is relatively simple, our reference model gives a reasonably good fit to PREM's profiles with a mean deviation less than $1\% \pm 0.4\%$ for V_S , and $1.0\% \pm 0.5\%$ for V_ϕ . Actually, we did not expect the seismic velocities of our reference model to match perfectly PREM. In fact, the assumption made in PREM of a Bullen parameter $\eta_B = \frac{dK_S}{dP} + \frac{1}{g} \frac{d(V_\phi^2)}{dr} = 1$ through all the lower mantle implies, among other things, that internal heating and the presence of thermal boundary layers are neglected [Poirier, 1991]. This assumption may not have a dramatic effect on densities, since the thermal expansion of the lower mantle is relatively small, but it can have an important effect on the elastic coefficients K and μ , and thus on V_P , V_S and V_ϕ . Furthermore, as pointed out by [Dewaele and Guyot, 1998], PREM underestimates the anelastic effects on seismic waves. This can also be seen in appendix D. Taking into account all these complications, we consider that our reference model is not incompatible with PREM.

3.3.7. Effect of thermodynamical parameters. The results previously described bear strong implications for understanding the structure and composition of the deep mantle. However, one should wonder to what extent our choice of model parameters affects our results. From the various laboratory studies and numerical simulations it is clear that the thermoelastic parameters and their derivatives for perovskite and magnesiowüstite are affected by significant uncertainties. To investigate the effect of these uncertainties on our results we can consider separately the effect of each thermoelastic parameter listed in Table 3. Reasonable variations of $K_T^{P_0, T_0}$ and μ^{P_0, T_0} will not affect significantly our results since it is the *variation* of these elastic coefficients with pressure and temperature which produces seismic velocity anomalies. The effect of iron on all elastic parameters is reported to be small, therefore, the relatively small increase of the iron content that we propose for parts the lowermost part of the mantle does not need to be considered. Thus, we can simply investigate the effect of pressure and temperature derivatives on the slope and position of the curve $d \ln V_\phi = 0$, because it determines the

composition of the dense material for a given chemical density contrast (see Plate 2). At a given depth the lateral variation of bulk sound speed is produced by temperature variations and composition at (almost) constant pressure, therefore slight variations of $(\partial\mu/\partial P)_T$ and $(\partial K/\partial P)_T$ parameters do not affect our results. Similarly, $(\partial\mu/\partial T)_P$ does not affect the curve $\text{dln}V_\phi=0$ since V_ϕ does not depend on μ . In contrast, the temperature variation of K has a considerable effect on the slope and on the position of the curve $\text{dln}V_\phi=0$.

For example, if $\delta T=400$ K, $KFe=3.5$ and $\Delta\rho_\chi/\rho = 1.7\%$ for the dense material, an increase of $(\partial K_S/\partial T)_P$ from -0.015 GPa K⁻¹ to -0.006 GPa K⁻¹ for the assemblage will require a decrease of xSi from 0.81 (see Table 4 or Plate 2b) to 0.75, with almost no change in xFe for the dense material. For the same conditions, a value of $(\partial K_S/\partial T)_P=-0.026$ GPa K⁻¹ for the assemblage yields $xSi=0.90$. Interestingly, in that case we have observed that a low value for KFe (0.5 instead of 3.5) reduces the required Si enrichment to 0.78.

The variations of $(\partial K_S/\partial T)_P$ investigated here are rather large compared to values that converges to ~ -0.015 GPa K⁻¹ (see appendix A). Still, it appears that the xSi value of the dense material is strongly correlated to this uncertainty.

4. DISCUSSION

A robust conclusion of our study is that the dense material must be enriched in both Fe and Si with respect to a pyrolitic composition as proposed by *Kellogg et al.* [1999], in order to satisfy geodynamical and seismological constraints. Several hypothesis can be advanced for such enrichment in Si and Fe.

(1) Subducted oceanic crust is enriched in Si and Fe and which was reported to be denser than a pyrolitic mantle at lower mantle pressures [*Hirose et al.*, 1999; *Guignot and Andrault*, 2004]. Indeed, the mineralogy of a MORB-type material becomes $\sim 30\%$ mol. of Al(Mg,Fe)-perovskite (with $xFe \sim 0.4$ and $xSi \sim 0.75$) and $\sim 20\%$ mol. of SiO₂ stishovite [*Guignot and Andrault*, 2004]. These iron and silica-rich phases could react with a pyrolitic mantle, yielding an enrichment in both Si and Fe. Following values listed in [*Guignot and Andrault*, 2004], $xSi_{pyrolite}/xSi_{MORB} \sim xFe_{pyrolite}/xFe_{MORB}$, where the subscript ‘MORB’ refers to Al(Mg,Fe)-perovskite and stishovite present in a MORB. To explain the highest enrichment in Si (i.e., $xSi=0.85$) and Fe (i.e., $xFe=0.17$, see Table 4) proposed in this study, about 30% vol. of subducted oceanic crust should be mixed with 70% vol. of pyrolitic mantle. Assuming a past subduction rate of ~ 30 km³/year and that the volume of the enriched material is 25% the whole mantle volume, the necessary amount of subducted oceanic crust would be reached after ~ 1.5 Gy of subduction.

(2) The iron enrichment could be due to the incorporation of iron from the outer core into the mantle [*Knittle and Jeanloz*, 1991], probably during the early stages of the Earth history, when convection was more vigorous.

(3) A previous experimental study [*Guyot et al.*, 1997] proposed that Si could be incorporated in Fe_{metal} at shallow depth and high temperature, during the early stages of core formation. At greater depth the Si incorporated in Fe_{metal} is no longer stable and SiO₂ would be formed [*Guyot et al.*, 1997]. This process could participate to the Si enrichment in the lowermost mantle.

(4) Another possibility is that the Earth’s bulk composition is not derived from CI chondrites, as generally assumed, but is derived from another type of material such as Enstatite chondrites, as proposed by *Javoy* [*Javoy*, 1995]. In such case, the bulk composition of the Earth could be depleted in Mg relative to a CI-derived bulk composition. Therefore, it would yield a Fe and Si-enriched lowermost mantle, since the upper part of the mantle is close to pyrolite.

5. CONCLUSIONS

Combining seismic tomography with geodynamical considerations provides a new way to constrain the nature of compositional heterogeneity in the lowermost mantle. We conducted thermochemical convection simulation, with a chemical density excess $\Delta\rho_\chi/\rho=1.7\%$ for the dense material, starting the calculation 2 Gy before present. After 2 Gy of convection, the dense hotter material develops a dynamical topography but remains stable in the lowermost mantle. Using a lower mantle thermodynamical model considering the assemblage of perovskite and magnesiowüstite, we constrain the composition of a dense material with respect to a reference mantle, assumed to have a pyrolitic composition. Available data and models are all compatible with the presence of a chemically denser material simultaneously enriched in Fe and Si. This enrichment is lower when the temperature contrast between the dense hotter material and the overlying mantle decreases.

We apply the composition which satisfies geodynamical and seismological constraints to the temperature and compositional fields extracted from convection simulations, and computed the main seismological parameters. Our results reproduce well seismological observations, in particular:

- (1) The presence of broad seismic velocity anomalies in the lowermost mantle.
- (2) The increase of the RMS seismic velocity anomalies below 2000 km depth.
- (3) The presence of anticorrelation between bulk sound speed and shear wave velocity anomalies, mainly located in upwelling areas.
- (4) The presence of areas of $R=\text{dln}V_S/\text{dln}V_P > 2.7$ that

match fairly well areas of anticorrelation between V_S and V_ϕ .

(5) The horizontally averaged R profile which increases below 2000 km to the CMB. When anelasticity is considered, R values are higher but anelasticity is not necessary to explain $R > 2.7$, unless if the latter are horizontally averaged. In that case, the strong lateral variations observed for composition and temperature can hide values of $R > 2.7$.

Several mechanisms can be advanced for the origin of a Si and Fe enrichment in the lowermost mantle such as the presence of subducted oceanic crust, the incorporation of Fe from the core in the early stages of Earth's mantle, chemical reactions between Si and Fe_{metal} , and/or a bulk composition of the Earth's mantle slightly different from the main canonical models.

APPENDIX A: CONVERSION FROM ISOTHERMAL TO ADIABATIC

Values for the isothermal bulk modulus K_T (Table 3) are converted to adiabatic bulk modulus K_S using:

$$K_S = K_T(1 + \alpha\gamma T), \quad (\text{A.1})$$

The thermodynamical Grüneisen parameter γ is volume dependent according to [Anderson, 1995]:

$$\gamma = \gamma_0 \left(\frac{\rho_0}{\rho} \right)^q, \quad (\text{A.2})$$

where the subscript 0 indicates reference ambient P and T . Under the quasi-harmonic approximation, the derivative of Equation A.1 with respect to temperature at constant P , yields :

$$\begin{aligned} \left(\frac{\partial K_S}{\partial T} \right)_P &= \left(\frac{\partial K_T}{\partial T} \right)_P (1 + \alpha\gamma T) \\ &+ K_T \alpha \gamma \left\{ 1 + T \left[\alpha q + \frac{1}{\alpha} \left(\frac{\partial \alpha}{\partial T} \right)_P \right] \right\}, \end{aligned} \quad (\text{A.3})$$

while the derivative with respect to pressure at constant T yields:

$$\begin{aligned} \left(\frac{\partial K_S}{\partial P} \right)_T &= \left(\frac{\partial K_T}{\partial P} \right)_T (1 + \alpha\gamma T) \\ &+ \gamma T \left[\frac{1}{K_T} \left(\frac{\partial K_T}{\partial T} \right)_P - \alpha q \right]. \end{aligned} \quad (\text{A.4})$$

For each of the two phases considered (i.e., perovskite and magnesiowüstite) we calculate the terms in Equations

A.3 and A.4 for ambient conditions using, in addition to Table 3, the following values of thermodynamical parameters: $\gamma_0^{pv}=1.33$ [Jackson and Rigden, 1996], $(\partial\alpha/\partial T)_P^{pv}=4.9 \cdot 10^{-8} \text{ K}^{-2}$ [Gillet et al., 2000], $\gamma_0^{mw}=1.41$ [Jackson and Rigden, 1996], $(\partial\alpha/\partial T)^{mw}=0.7 \cdot 10^{-8} \text{ K}^{-2}$ [Suzuki, 1975]. Equation 15 provides $\alpha_0^{pv}=2.6 \cdot 10^{-5} \text{ K}^{-1}$ and $\alpha_0^{mw}=4.1 \cdot 10^{-5} \text{ K}^{-1}$, and q is close to one for both phases. This yields $(\partial K_S)/(\partial T)_P^{pv}=-0.015 \text{ GPa K}^{-1}$ and $(\partial K_S)/(\partial T)_P^{mw}=-0.019 \text{ GPa K}^{-1}$, in good agreement with [Jackson, 1998; Gillet et al., 2000] for perovskite and with [Sunmino et al., 1983; Isaak et al., 1989] for magnesiowüstite. We obtain $(\partial K_S)/(\partial P)_T=4.09$ for perovskite and $(\partial K_S)/(\partial P)_T=4.03$ for magnesiowüstite, values that are slightly different from the isothermal case, as reported by [Dewaele and Guyot, 1998].

APPENDIX B: PRESSURE DEPENDENCE OF C_P

The pressure dependence of the specific heat $C_P = T(\partial S)/(\partial T)_P$ is expressed as follows:

$$C_P^P = C_P^{P_0} + \left(\frac{\partial C_P}{\partial P} \right)_T (P - P_0). \quad (\text{B.1})$$

The pressure dependence of C_P writes:

$$\left(\frac{\partial C_P}{\partial P} \right)_T = T \frac{\partial}{\partial T} \left(\left(\frac{\partial S}{\partial P} \right)_T \right)_P \quad (\text{B.2})$$

Using the Maxwell relationship $(\partial S)/(\partial P)_T = -(\partial V)/(\partial T)_P = \alpha V$ (V being the volume) one gets:

$$\left(\frac{\partial C_P}{\partial P} \right)_T = -TV \left[\left(\frac{\partial \alpha}{\partial T} \right)_P + \alpha^2 \right] \quad (\text{B.3})$$

Therefore Equation B.3 gives the pressure dependence of C_P . For simplicity we assume that $(\partial C_P)/(\partial P)_T$ is constant and we choose the value at ambient conditions.

APPENDIX C: SEISMIC FILTERING

Our seismic filter is a moving average Gaussian operator [Vacher et al., 1996]:

$$\begin{aligned} d \ln V(x, z) &= d \ln V(x_0, z_0) \\ &\exp \left\{ -\frac{1}{2} \left[\left(\frac{x - x_0}{L_x} \right)^2 + \left(\frac{z - z_0}{L_z} \right)^2 \right] \right\}, \end{aligned} \quad (\text{C.1})$$

$d \ln V(x_0, z_0)$ is the velocity anomaly at the center of the moving window. The horizontal and vertical correlation lengths, L_x and L_z are taken equal to 180 km.

APPENDIX D: SEISMIC ATTENUATION

At a given pressure and for a weak anelasticity, the effect of seismic attenuation on seismic velocities can be expressed as follows [Karato, 1993]:

$$V(w, T) = V_0(T) \left[1 - \frac{1}{2Q(w, T)} \cotan \left(\frac{a\pi}{2} \right) \right]. \quad (\text{D.1})$$

The attenuation of seismic waves is then given by the inverse of Q , the quality factor, which depends on the frequency w of seismic waves and on temperature T according to [Karato and Karki, 2001]:

$$Q(w, T) \sim w^{\alpha_a} \exp \left(\frac{\alpha_a \beta T_m}{T} \right). \quad (\text{D.2})$$

α_a and β are non dimensional constants, the latter depending on the activation enthalpy H^* according to $H^* = \beta R_c T_m$, with R_c the gas constant and T_m the melting temperature of the material considered. Following [Wang, 1999] the pressure dependence of T_m was estimated by integrating Lindemann law:

$$T_m = T_{m_0} \exp \left[2\gamma_S \left(1 - \frac{\rho_0}{\rho} \right) + \frac{2}{3} \ln \left(\frac{\rho_0}{\rho} \right) \right], \quad (\text{D.3})$$

with the Slater gamma $\gamma_S = \frac{1}{2} \left(\frac{dK_T}{dP} - \frac{1}{3} \right)$. We take $T_{m_0} = T_m(P_0, T_0) = 2800$ K for both perovskite and magnesiowüstite [Wang, 1999; Anderson, 1995], $w = 0.25$ Hz (i.e., a period of 4s), $\alpha_a = 0.2$ for the assemblage [Karato and Karki, 2001]. Taking $H^* = 230$ kJ/mol for magnesiowüstite and $H^* \sim 300$ kJ/mol for perovskite (according to values listed in [Karato and Karki, 2001]) we obtain $\beta^{mw} = 9.9$ and $\beta^{pv} = 12.9$. For the assemblage of the two phases we calculate β by doing a simple Voigt average. Assuming a constant volumic proportion of perovskite $\varphi = 0.85$, we obtain $\beta = 12.5$ for the assemblage. Figure 4 shows the calculated shear quality factor average profile for our reference mantle and for our geodynamical model. Due to the decrease of Q in the lowermost mantle induced by temperature, attenuation becomes more important in the dense hotter material. Note that the shear quality factor for our reference model significantly differs from PREM which assumes that $Q = 312$ through all the lower mantle.

Acknowledgments. We thank Laurent Guillot, François Guyot, Stéphane Labrosse and Barbara Romanowicz for stimulating discussions and useful advice. We are grateful to Paul Tackley for providing his numerical code. Comments by Bradford Hager, Jan Matas and an

anonymous reviewer significantly improved the first version of this manuscript. Figures were made with the Generic Mapping Tools (P. Wessel and W.H.F Smith, EOS, Trans. AGU 76 (1995) 329).

REFERENCES

- Anderson, O. L., *Equations of State of Solids for Geophysics and Ceramic Science*, vol. 81, Oxford monographs on geology and geophysics, 1995.
- Anderson, O. L., H. Oda, and D. Isaak, A model for the computation of thermal expansivity at high compression and high temperatures: MgO as an example, *Geophys. Res. Lett.*, 19, 1987–1990, 1992.
- Andrault, D., Evaluation of (Mg, Fe) partitioning between silicate perovskite and magnesiowüstite up to 120 GPa and 2300 K, *J. Geophys. Res.*, 106, 2079–2087, 2001.
- Antolik, M., Y. J. Gu, G. Ekström, and A. M. Dziewonski, J362D28: a new joint model of compressional and shear velocity in the Earth’s mantle, *Geophys. J. Int.*, 153, 443–466, 2003.
- Birch, F., Elasticity and constitution of the Earth’s interior, *J. Geophys. Res.*, 57, 227–286, 1952.
- Bréger, L., B. Romanowicz, and L. Vinnick, Test of tomographic models of D” using differential travel time data, *Geophys. Res. Lett.*, 25, 5–8, 1998.
- Bréger, L., B. Romanowicz, and C. Ng, The Pacific plume as seen by S, ScS, and SKS, *Geophys. Res. Lett.*, 28, 1859–1862, 2001.
- Brown, J. M., and T. J. Shankland, Thermodynamic parameters in the Earth as determined from seismic profiles, *Geophys. J. R. Astron. Soc.*, 66, 579–596, 1981.
- Chopelas, A., and R. Boehler, Thermal expansivity in the lower mantle, *J. Geophys. Res.*, 19, 1983–1986, 1992.
- Davies, G. F., Effective elastic moduli under hydrostatic stress. 1. Quasi-harmonic theory, *J. Phys. Chem. Solids.*, 35, 1513–1520, 1974.
- Deschamps, F., and J. Trampert, Mantle tomography and its relation to temperature and composition, *Phys. Earth. Pl. Int.*, 140, 277–291, 2003.
- Dewaele, A., and F. Guyot, Thermal parameters of the Earth’s lower mantle, *Phys. Earth. Pl. Int.*, 107, 261–267, 1998.
- Duffy, T. S., and D. L. Anderson, Seismic velocities in mantle minerals and the mineralogy of the upper mantle, *J. Geophys. Res.*, 94, 1895–1912, 1989.

- Dziewonski, A. M., and D. L. Anderson, Preliminary reference Earth model, *Phys. Earth. Pl. Int.*, 25, 297–356, 1981.
- Farnetani, C. G., Excess temperature of mantle plumes : The role of chemical stratification across D", *Geophys. Res. Lett.*, 24, 1,583–1,586, 1997.
- Farnetani, C. G., and H. Samuel, Lagrangian structures and stirring in the Earth's mantle, *Earth Planet. Sci. Lett.*, 206, 335–348, 2003.
- Fiquet, G., A. Dewaele, D. Andrault, M. Kunz, and T. Le Bihan, Thermoelastic properties and crystal structure of MgSiO₃ perovskite at lower mantle pressure and temperature conditions, *Geophys. Res. Lett.*, 27, 21–24, 2000.
- Forte, A. M., and J. X. Mitrovica, Deep-mantle high-viscosity flow and thermochemical structure inferred from seismic and geodynamic data, *Nature*, 410, 1049–1056, 2001.
- Gillet, P., I. Daniel, F. Guyot, J. Matas, and J.-C. Chervin, A thermodynamic model for MgSiO₃-perovskite derived from pressure, temperature and volume dependence of the raman mode frequencies, *Phys. Earth. Pl. Int.*, 117, 361–384, 2000.
- Grand, S. P., R. D. van der Hilst, and S. Widiyantoro, High resolution global tomography: A snapshot of convection in the Earth, *Geol. Soc. Am. Today*, 7, 1–7, 1997.
- Guignot, N., and D. Andrault, Equations of state of Na-K-Al host phases and implications for MORB density in the lower mantle, *Phys. Earth. Pl. Int.*, 143-144, 107–128, 2004.
- Guyot, F., M. Madon, J. Peyronneau, and J.-P. Poirier, X-ray microanalysis of high-pressure/high-temperature phases synthesized from natural olivine in a diamond-anvil cell, *Earth Planet. Sci. Lett.*, 90, 52–64, 1988.
- Guyot, F., J. Zhang, I. Martinez, J. Matas, Y. Ricard, and M. Javoy, P-V-T measurements of iron silicide (ϵ -FeSi). Implications for silicate-metal interactions in the early Earth, *Eur. J. Mineral.*, 9, 277–285, 1997.
- Hama, J., and K. Suito, Thermoelastic properties of periclase and magnesiowüstite under high pressure and temperature, *Phys. Earth. Pl. Int.*, 114, 165–179, 1999.
- Hirose, K. Y., Y. M. A. Fei, and H. K. Mao, The fate of subducted basaltic crust in the Earth's lower mantle, *Nature*, 397, 53–56, 1999.
- Hofmann, A. W., Mantle geochemistry: the message from oceanic volcanism, *Nature*, 385, 219–229, 1997.
- Isaak, D. G., O. L. Anderson, and T. Goto, Measured elastic modulus of single-crystal MgO up to 1800 K, *Phys. Chem. Miner.*, 16, 703–704, 1989.
- Ishii, M., and J. Tromp, Normal-mode and free-air gravity constraints on lateral variations in velocity and density of Earth's mantle, *Science*, 285, 1231–1236, 1999.
- Jackson, I., Elasticity, composition and temperature of the Earth's lower mantle: a reappraisal, *Geophys. J. Int.*, 134, 291–311, 1998.
- Jackson, I., and S. M. Rigden, Analysis of P-V-T data: constraints on the thermoelastic properties of high-pressure minerals, *Phys. Earth. Pl. Int.*, 96, 85–112, 1996.
- Javoy, M., The integral enstatite chondrite model of the Earth, *Geophys. Res. Lett.*, 22, 2219–2222, 1995.
- Karato, S.-I., Importance of anelasticity in the interpretation of seismic tomography, *Geophys. Res. Lett.*, 20, 1623–1626, 1993.
- Karato, S.-I., and B. B. Karki, Origin of lateral variation of seismic wave velocities and density in the deep mantle, *J. Geophys. Res.*, 106, 21,771–21,783, 2001.
- Karki, B. B., and L. Stixrude, Seismic velocities of major silicate and oxide phases of the lower mantle, *J. Geophys. Res.*, 104, 13,025–13,033, 1999.
- Kellogg, L. H., B. H. Hager, and R. D. van der Hilst, Compositional stratification in the deep mantle, *Science*, 283, 1,881–1,884, 1999.
- Kennett, B. L. N., S. Widiyantoro, and R. D. van der Hilst, Joint seismic tomography for bulk sound and shear wave speed in the Earth's mantle, *J. Geophys. Res.*, 103, 12,469–12,493, 1998.
- Knittle, E., and R. Jeanloz, Earth's core-mantle boundary: Results of experiments at high pressures and temperatures, *Science*, 251, 1,438–1,443, 1991.
- Lebars, M., and A. Davaille, Stability of thermal convection in two superimposed miscible viscous fluids, *J. Fluid Mech.*, 471, 339–363, 2002.
- Li, X., and B. Romanowicz, Global mantle shear velocity model developed using nonlinear asymptotic coupling theory, *J. Geophys. Res.*, 101, 22,245–22,272, 1996.
- Masters, G., G. Laske, H. Bolton, and A. M. Dziewonski, The relative behavior of shear velocity, bulk sound speed and compressional velocity in the mantle: implication for

- chemical and thermal structure, in *Earth's deep interior. Mineral physics and tomography from the atomic to the global scale*, vol. 117, edited by S.-I. Karato, A. Forte, R. C. Liebermann, G. Masters, and L. Stixrude, pp. 63–87, American Geophysical Union, Washington, DC, 2000.
- Matsui, M., Molecular dynamics simulation of MgSiO₃ perovskite and the 660-km seismic discontinuity, *Phys. Earth. Pl. Int.*, *121*, 77–84, 2000.
- McDonough, W. F., and S. Sun, The composition of the Earth, *Chem. Geol.*, *120*, 223–253, 1995.
- Meade, C., P. G. Silver, and S. Kaneshima, Laboratory and seismological observations of lower mantle anisotropy, *Geophys. Res. Lett.*, *22*, 1293–1296, 1995.
- Mégnin, C., and B. Romanowicz, The three-dimensional shear velocity structure of the mantle from the inversion of body, surface and higher-mode waveforms, *Geophys. J. Int.*, *143*, 709–728, 2000.
- Poirier, J.-P., *Introduction to the physics of the Earth's interior*, Cambridge University Press, 1991.
- Robertson, G. S., and J. H. Woodhouse, Ratio of relative S to P heterogeneity in the lower mantle, *J. Geophys. Res.*, *101*, 20,041–20,052, 1996.
- Romanowicz, B., Can we resolve 3D density heterogeneity in the lower mantle?, *Geophys. Res. Lett.*, *6*, 1107–1110, 2001.
- Saltzer, R. L., R. D. van der Hilst, and H. Kàrason, Comparing P and S wave heterogeneity in the mantle, *Geophys. Res. Lett.*, *28*, 1335–1338, 2001.
- Samuel, H., and C. G. Farnetani, Thermochemical convection and helium concentrations in mantle plumes, *Earth Planet. Sci. Lett.*, *207*, 39–56, 2003.
- Sidorin, I., and M. Gurnis, Geodynamically consistent seismic velocity predictions at the base of the mantle, in *The Core-mantle Boundary Region*, edited by M. Gurnis, M. E. Wysession, E. Knittle, and B. A. Buffett, pp. 209–230, American Geophysical Union, Washington, DC, 1998.
- Sinelnikov, Y. D., G. Chen, D. R. Neuville, M. T. Vaughan, and R. C. Liebermann, Ultrasonic shear wave velocities of MgSiO₃ perovskite at 8 GPa and 800 K and lower mantle composition, *Science*, *281*, 677–679, 1998.
- Stacey, F. D., and P. M. Davis, High pressure equations of state with applications to the lower mantle and core, *Phys. Earth. Pl. Int.*, *142*, 137–184, 2004.
- Su, W., and A. M. Dziewonski, Predominance of long-wavelength heterogeneity in the mantle, *Nature*, *352*, 121–126, 1991.
- Sunmimo, Y., O. L. Anderson, and Y. Suzuki, Temperature coefficients of single cristal MgO between 80 and 1300 K, *Phys. Chem. Miner.*, *9*, 38–47, 1983.
- Suzuki, I., Thermal expansion of periclase and olivine, and their anharmonic properties, *J. Phys. Earth*, *23*, 145–159, 1975.
- Tackley, P. J., Strong heterogeneity caused by deep mantle layering, *Geochem. Geophys. Geosyst.*, *3*(4), 10.1029/2001GC000167, 2002.
- Turcotte, D. L., and G. Schubert, *Geodynamics : Application of continuum physics to geological problems*, John Wiley, New York, 1982.
- Vacher, P., A. Mocquet, and C. Sotin, Comparison between tomographic structures and models of convection in the upper mantle, *Geophys. J. Int.*, *124*, 45–56, 1996.
- van der Hilst, R. D., S. Widiyantoro, and E. R. Engdahl, Evidence for deep mantle circulation from global tomography, *Nature*, *386*, 578–584, 1997.
- Wang, Y., and D. J. Weidner, $(\partial\mu/\partial T)_P$ of the lower mantle, *Pure Appl. Geophys.*, *146*, 533–549, 1996.
- Wang, Z. W., The melting of Al-bearing perovskite at the core mantle boundary, *Phys. Earth. Pl. Int.*, *115*, 219–228, 1999.
- Watt, J., G. Davies, and R. O'Connell, The elastic properties of composite materials, *Rev. Geophys. Space Phys.*, *14*, 541–563, 1976.
- Yeganeh-Haeri, A., Synthesis and re-investigation of the elastic properties of single-crystal magnesium silicate perovskite, *Phys. Earth. Pl. Int.*, *87*, 111–121, 1994.
- Zhong, S., and B. H. Hager, Entrainment of a dense layer by thermal plumes, *Geophys. J. Int.*, *154*, 666–676, 2003.

D. Andrault, Institut de Minéralogie et de Physique des Milieux Condensés, Paris 6, Campus Boucicaut, Bat. 7, 140 rue de Lourmel, 75015 Paris (dandrault@ipgp.jussieu.fr)

C. G. Farnetani, Laboratoire de Dynamique des Systèmes Géologiques, Institut de Physique du Globe de Paris, 4 place jussieu, B.P. 89, 75252 Paris CEDEX 05, France. (cinzia@ipgp.jussieu.fr)

H. Samuel, Department of Geology and Geophysics, Kline Geology Laboratory, Yale University, P.O. Box 208109, New Haven, CT 06520-8109, USA. (henri.samuel@yale.edu)

Table 1. Iron dependence of physical parameters for perovskite and magnesiowüstite ([Wang and Weidner, 1996] and references therein).

Table 1. Iron dependence of physical parameters for perovskite and magnesiowüstite ([Wang and Weidner, 1996] and references therein).

Parameters	Mg _{x_{Mg}} Fe _{x_{Fe}} SiO ₃	Mg _{x_{Mg}} Fe _{x_{Fe}} O
$K_0(x_{Fe})(\text{GPa})$	$K_0(0)$	$K_0(0) + 7.5x_{Fe}$
$\mu_0(x_{Fe})(\text{GPa})$	-	$\mu_0(0) + 77.0x_{Fe}$
$\rho_0(x_{Fe})(\text{kg/m}^3)$	$4108 + 1070x_{Fe}$	$3583 + 2280x_{Fe}$
$V_0(x_{Fe}) (\text{cc/mol})$	$24.46 + 1.03x_{Fe}$	$11.25 + 1.00x_{Fe}$

Table 2. Model parameters

Table 2. Model parameters

Parameter	Surface value	Bottom value	Unit
T	300	3470	K
Di	0.65	0.35	-
γ	1.33	1.01	-
α	$2.7 \cdot 10^{-5}$	$0.9 \cdot 10^{-5}$	K^{-1}
ρ	4160	5620	kg m^{-3}
k	3	5.4	W m^{-1}

Table 3. Isothermal elastic constants of Mg-perovskite and periclase and their first order P and T derivatives, from [Matsui, 2000], except value with * (see text).

Table 3. Isothermal elastic constants of Mg-perovskite and periclase and their first order P and T derivatives, from [Matsui, 2000], except value with * (see text).

	MgSiO ₃	MgO
$K_T^{P_0, T_0} (\text{GPa})$	258.1	161.0
$\mu^{P_0, T_0} (\text{GPa})$	176.8	131.0
$\left(\frac{\partial K_T}{\partial T}\right)_P (\text{GPa K}^{-1})$	-0.029	-0.028
$\left(\frac{\partial K_T}{\partial P}\right)_T$	4.1	4.05
$\left(\frac{\partial \mu}{\partial T}\right)_P (\text{GPa K}^{-1})$	-0.024*	-0.024
$\left(\frac{\partial \mu}{\partial P}\right)_T$	1.4	2.4

Table 4. Compositions of the dense material which satisfies geodynamical and seismological considerations for different chemical density contrasts and temperature contrasts with respect to a reference pyrolitic mantle, at $P=100$ GPa.

Table 4. Compositions of the dense material which satisfies geodynamical and seismological considerations for different chemical density contrasts and temperature contrasts with respect to a reference pyrolitic mantle, at $P=100$ GPa.

$\Delta\rho_\chi/\rho$	δT (K)	KFe	xSi	xFe
1%	400	3.5	0.77	0.14
1%	800	3.5	0.80	0.14
1.7%	400	3.5	0.81	0.17
1.7%	800	3.5	0.85	0.17

Plate 1. (a) Non dimensional potential temperature field and velocity field at present day time; (b) Corresponding compositional field, $\chi > 0$ indicates chemically dense material; (c) Seismic velocity anomalies for bulk sound and (d) for shear wave. (e) Areas of anticorrelation between positive bulk sound and negative shear wave velocity anomalies (grey). (f) Areas where $R=d\ln V_S/d\ln V_P > 2.7$ (grey).

Plate 1. (a) Non dimensional potential temperature field and velocity field at present day time; (b) Corresponding compositional field, $\chi > 0$ indicates chemically dense material; (c) Seismic velocity anomalies for bulk sound and (d) for shear wave. (e) Areas of anticorrelation between positive bulk sound and negative shear wave velocity anomalies (grey). (f) Areas where $R=d\ln V_S/d\ln V_P > 2.7$ (grey).

Figure 1. Depth profiles: (a) Temperature profile at present day time for our geodynamical model (plain) and for our reference model (dashed). (b) Density profile for our reference mantle (plain) and PREM density profile (dashed). (c) Thermal expansion coefficient for our reference pyrolitic mantle, for perovskite (dashed), magnesiowüstite (dotted) and the whole assemblage (plain).

Figure 1. Depth profiles: (a) Temperature profile at present day time for our geodynamical model (plain) and for our reference model (dashed). (b) Density profile for our reference mantle (plain) and PREM density profile (dashed). (c) Thermal expansion coefficient for our reference pyrolitic mantle, for perovskite (dashed), magnesiowüstite (dotted) and the whole assemblage (plain).

Figure 2. Comparison of horizontally averaged quantities calculated with the numerical convection code (dashed lines) and our post-processing calculations (solid lines). (a) Effective buoyancy number $B_{eff} = \Delta\rho_\chi/(\rho\alpha(T - T_0))$. (b) Chemical density contrast $\Delta\rho_\chi/\rho$ at ambient temperature.

Figure 2. Comparison of horizontally averaged quantities calculated with the numerical convection code (dashed lines) and our post-processing calculations (solid lines). (a) Effective buoyancy number $B_{eff} = \Delta\rho_\chi/(\rho\alpha(T - T_0))$. (b) Chemical density contrast $\Delta\rho_\chi/\rho$ at ambient temperature.

Plate 2. Compositions of the dense material (xFe and xSi). All calculations are performed at $P=100$ GPa and $T=2200$ K. Blue curve: $d\ln V_S=0$, above it $d\ln V_S < 0$. Red curve: $d\ln V_\phi=0$, above it $d\ln V_\phi < 0$. Grey areas: compositions of the dense material which produce $d\ln V_\phi/d\ln V_S < 0$. Light grey area: compositions that satisfy simultaneously $d\ln V_\phi/d\ln V_S < 0$ and $d\ln V_S < 0$ (see text). Blue triangle: assumed pyrolitic composition of reference mantle. Black lines: isocontours of chemical density contrasts at ambient temperature $\Delta\rho_\chi/\rho$ at 0%, 1%, 2% and 4%, green line: $\Delta\rho_\chi/\rho=1.7\%$ corresponds to our geodynamical model. Orange area: the compositions that satisfy both geodynamical and seismological constraints (see text). Crosses: composition of the dense material which satisfies simultaneously $\Delta\rho_\chi/\rho=1.7\%$, $d\ln V_\phi/d\ln V_S < 0$, $d\ln V_S < 0$ and which differs the least from a pyrolitic composition. (a) $\delta T=400$ K and $KFe=3.5$; (b) $\delta T=800$ K and $KFe=3.5$ (See text).

Plate 2. Compositions of the dense material (xFe and xSi). All calculations are performed at $P=100$ GPa and $T=2200$ K. Blue curve: $d\ln V_S=0$, above it $d\ln V_S < 0$. Red curve: $d\ln V_\phi=0$, above it $d\ln V_\phi < 0$. Grey areas: compositions of the dense material which produce $d\ln V_\phi/d\ln V_S < 0$. Light grey area: compositions that satisfy simultaneously $d\ln V_\phi/d\ln V_S < 0$ and $d\ln V_S < 0$ (see text). Blue triangle: assumed pyrolitic composition of reference mantle. Black lines: isocontours of chemical density contrasts at ambient temperature $\Delta\rho_\chi/\rho$ at 0%, 1%, 2% and 4%, green line: $\Delta\rho_\chi/\rho=1.7\%$ corresponds to our geodynamical model. Orange area: the compositions that satisfy both geodynamical and seismological constraints (see text). Crosses: composition of the dense material which satisfies simultaneously $\Delta\rho_\chi/\rho=1.7\%$, $d\ln V_\phi/d\ln V_S < 0$, $d\ln V_S < 0$ and which differs the least from a pyrolitic composition. (a) $\delta T=400$ K and $KFe=3.5$; (b) $\delta T=800$ K and $KFe=3.5$ (See text).

Figure 3. (a) RMS seismic velocity anomaly profiles calculated for V_S (solid line), V_P (dotted line) and V_ϕ (dashed line). (b) Horizontally averaged $R=d\ln V_S/d\ln V_P$ profile for our model, without anelastic effects (dashed line), with anelastic effects (dotted line). The maximum R values are plotted for the case where anelastic effects are not considered (solid line). The grey area corresponds to $R > 2.7$

Figure 3. (a) RMS seismic velocity anomaly profiles calculated for V_S (solid line), V_P (dotted line) and V_ϕ (dashed line). (b) Horizontally averaged $R=d\ln V_S/d\ln V_P$ profile for our model, without anelastic effects (dashed line), with anelastic effects (dotted line). The maximum R values are plotted for the case where anelastic effects are not considered (solid line). The grey area corresponds to $R > 2.7$

Figure 4. Horizontally averaged profile of shear quality factor, for our reference mantle (dashed line) and for our model (solid line).

Figure 4. Horizontally averaged profile of shear quality factor, for our reference mantle (dashed line) and for our model (solid line).

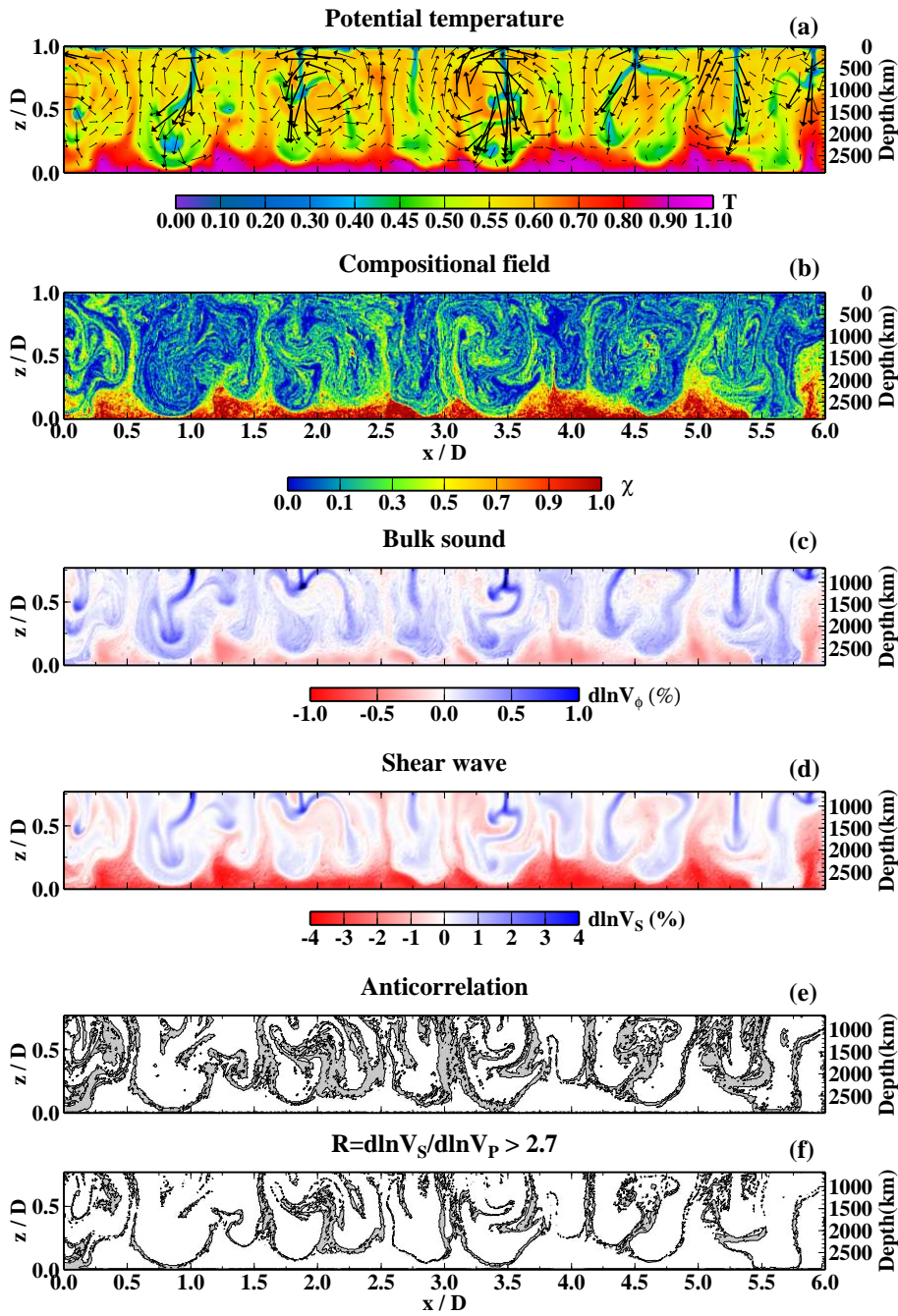


Plate 1

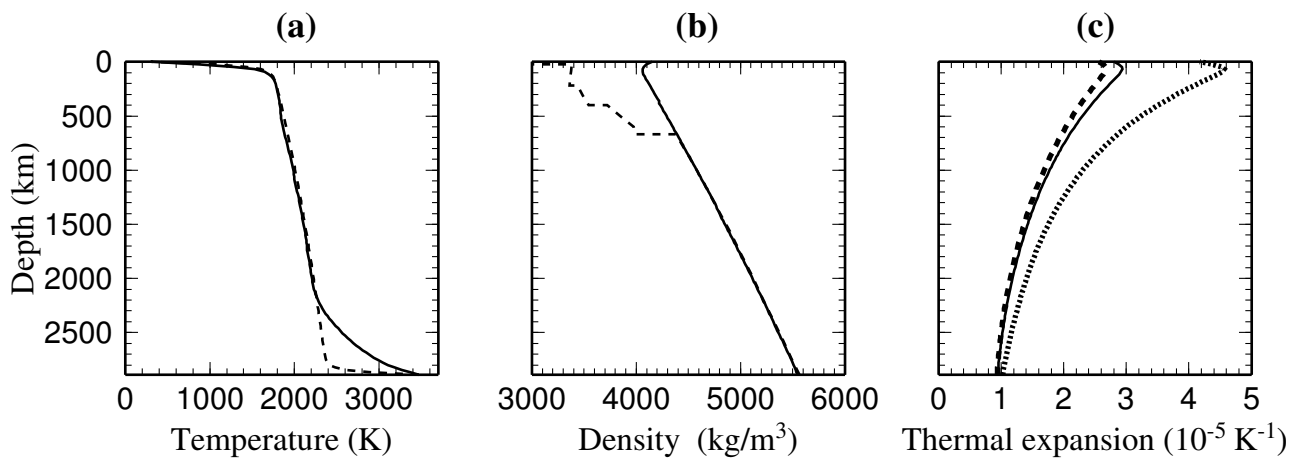
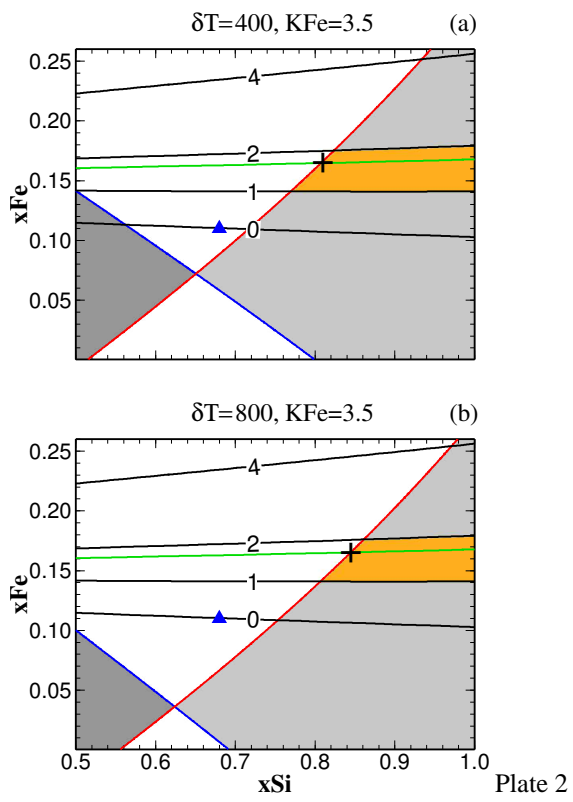


Figure 1

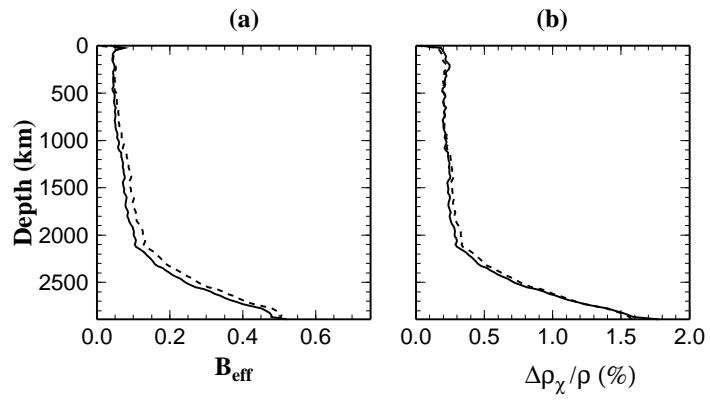


Figure 2

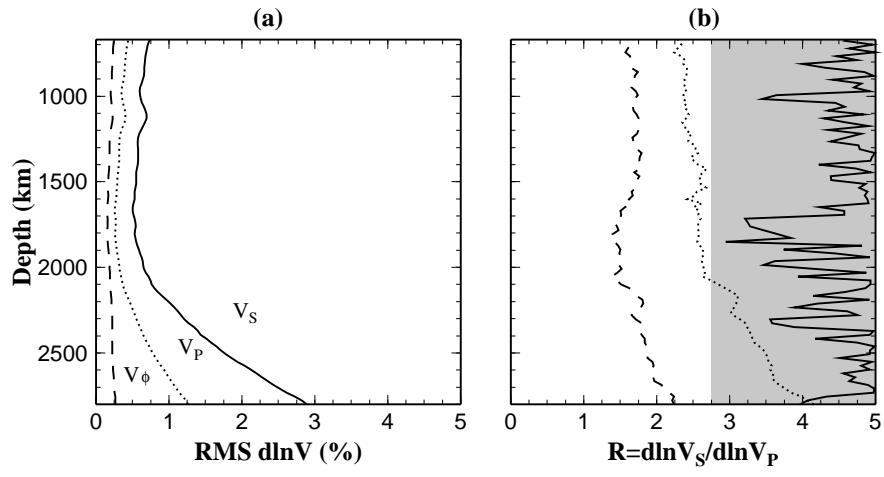


Figure 3

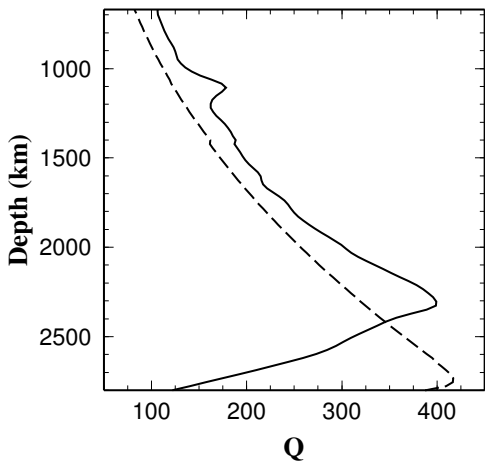


Figure 4